Fast and selective isoprene gas sensor: Influence of polystyrene size and role of the au catalyst on gas sensing properties

Junho Hwang [a],[1], See-Hyung Park [b],[1], Young-Seok Shim [b],[1], Sungwoo Sohn [a], Jae Han Chung [b], Yun-Haeng Cho [b], Jinho Lee [c], Myungwoo Choi [d], Gye Hyeon Lee [e], Donghwi Cho [e],[f],[*], Kwangjae Lee [g],[**], Wooyoung Lee [a],[**]

[a] Department of Materials Science and Engineering, Yonsei University, Seoul 03722, Republic of Korea
[b] School of Energy, Materials and Chemical Engineering, Korea University of Technology and Education (KOREATECH), Cheonan 31253, Republic of Korea
[c] Department of Materials Science and Engineering, Korea Advanced Institute of Science and Technology (KAIST), Daejeon 34141, Republic of Korea
[d] Department of Materials Science and Engineering, Korea University, Seoul 02841, Republic of Korea
[e] Thin Film Materials Research Center, Korea Research Institute of Chemical Technology (KRICT), Daejeon 34114, Republic of Korea
[f] Advanced Materials and Chemical Engineering, University of Science and Technology, Daejeon 34113, Republic of Korea
[g] Department of Information Security Engineering, Sangmyung University, Cheonan 31066, Republic of Korea

ARTICLE INFO

ABSTRACT

Sacrificial methods using polystyrene (PS) templates are extensively applied in various research fields, particularly for fabricating gas sensors. The many processing advantages of these methods, such as a uniform particle size distribution, ease of manipulation, and potential for functionalization enable the fabrication of intricate nanostructures with precise control of the geometry and surface-area-to-volume ratio. Nevertheless, no previous study has investigated the fundamental correlation between the size of the PS particles used as a template and the performance of the resulting functional gas sensor. In this study, we fabricated In$_2$O$_3$ hollow hemispheres (HHs) with PS template sizes ranging from 200 to 3000 nm to explore the essential aspects for gas sensor applications. Notably, compared to In$_2$O$_3$ thin films, In$_2$O$_3$ HHs-based sensors prepared using a 3000 nm PS template exhibited a larger surface area, particularly when formed in a monolayer, and achieved an enhanced gas response to C$_2$H$_5$OH by approximately 132 times. By decorating In$_2$O$_3$ HHs with Au nanoparticles, the detection of C$_5$H$_8$ at 350 °C among various volatile organic compounds was significantly enhanced (increase ratio = 31.7), achieving a response of 483 and a theoretical detection limit as low as 743 parts per trillion (ppt). In addition, the highly porous structure with Au decoration achieved an extremely short response time of less than 2 s. These unprecedented results provide critical insights into conventional sensor technologies and pave the way for potential health-monitoring applications and bioelectronics.

1. Introduction

Micro/nanomaterials are significant for diverse technological applications and scientific disciplines owing to the emergence of distinctive properties or behaviors at the sub-100 nm to micron scale that are distinct from those exhibited by macroscopic materials [1–10]. The realization of these advantageous properties necessitates meticulous control over various aspects of material design [4,6,11,12], including the composition [13,14], feature dimensions [4,6,15–17], shape [18–20], and local chemical environments [21,22]. Colloidal synthesis and subsequent particle assembly have shown promise as an appealing strategy for material development [23–25] based on its scalability and ability to develop general model systems. This approach facilitates an in-depth exploration of the physicochemical interactions of the final

structures with their surrounding environments [25], offering insights applicable to research domains such as photonic crystals [26], meta-materials [27], energy systems [28], and sensors [25,29].

The self-assembly of polystyrene (PS) nanoparticles via colloidal methods is a promising approach for constructing templates for functionalizing materials [30–32]. Notably, in the context of gas-sensor applications, semiconducting metal oxide (SMO) nanostructures derived from PS templates exhibit notable characteristics such as highly porous and interconnected structures with inverse opal and nanodome-like structures [11,25,29,33,34]. These structures exhibit advantageous features for sensor design, including a substantial surface area favorable for enhancing the chemical reactions between the SMO and target gaseous chemical molecules, facile control over structural parameters, operational simplicity, and cost-effectiveness [25,29]. For example, Cho *et al.* reported bimodal pore-loaded hierarchical SnO_2 spheres, obtained by the use of electrostatic sprayed PS templates [35]. The resultant pore-loaded hierarchical 3D SnO_2 spheres were employed as sensing layers for detecting acetone, and showed an enhanced response, approximately 20 % higher than that of hierarchical SnO_2 spheres without additional nanopores. Yi *et al.* produced heterojunctions of NiO nanoigloos adorned with inner-/outer sided tungsten using a combination of radio frequency sputtering and soft-template approaches [18]. By exploiting the morphological changes achieved through controlled deposition conditions, the utility factor, transducer function, and receptor function of the NO_2 sensor were comprehensively investigated.

Although numerous studies have utilized the aforementioned strategies to elevate the sensor performance to a commercial standard, there is a notable gap in the literature concerning the particle size effect of PS templates [20]. Since the PS size determines the microscopic structure/morphology and plays a fundamental role in sensor performance, it is imperative to understand the functional nanostructure generated through morphological evolution with different PS template sizes. The insights into the size effects of PS templates extend beyond sensor-based fields and would also benefit various applications in nanoelectronics [36].

Here, we explored the impact of the PS template particle size (200–3000 nm) on gas-sensor performance to enhance the geometric factors in chemoresistive gas sensors fabricated using PS templates. A representative n-type oxide, In_2O_3 (150 nm thickness), known for its sensing stability and reliability [37–41], was deposited on a monolayered PS template. Following template removal, the gas-sensing performance, including the gas response, selectivity, and response stability, was assessed upon exposure to the target gas molecules. Additionally, decoration with Au nanoparticles (NPs) exhibited a pronounced catalytic effect on C_5H_8 (isoprene) gas [42], displaying a high response of 483, a theoretical limit of detection down to 743 parts per trillion (ppt), and exceptional selectivity toward common volatile organic compounds. Contrary to expectations, our experiments revealed that the sensor fabricated using the 3,000-nm template outperformed those formed using smaller template particles. This observation is attributed to the dominance of the surface area in governing the overall sensing performance, particularly in the context of monolayer systems, rather than to the number of double Schottky barriers. Experimental measurements and sensor kinetic analysis substantiated the findings related to the optimal size of the PS templates. The high performance demonstrated by the optimal sensor highlights its potential application in bioelectronics for next-generation health monitoring.

2. Experimental Section

2.1. Sample fabrication

Platinum interdigitated electrodes (IDEs) were fabricated using photolithography and e-beam evaporation techniques [4]. A SiO_2/Si substrate was sequentially cleaned with acetone, isopropanol, and deionized water using a sonicator for 5 min each. Subsequently, a layer of photoresist (LOR 5 A, MicroChem Corporation) was spin-coated onto the Si wafer at 3000 rpm for 30 s. After baking at 190 °C for 5 min, another photoresist (AZ GXR 601, AZ Electronic Materials) was spin-coated onto the Si wafer at 3000 rpm for 30 s. Subsequently, after baking at 150 °C for 1 min, patterning of the IDEs was performed using a mask aligner system (MDA-400S, MIDAS System). After developing the patterned Si wafer (AZ 300MIF, MicroChemicals) and rinsing with deionized water, the wafer was subjected to photolithography and loaded into an e-beam evaporator (EBX-1000, ULVAC) to deposit Pt/Ti (180 nm/20 nm). The Pt-IDE-patterned SiO_2/Si substrate was subjected to UV/ozone cleaning (AC-6, Ah Tech LTS) for 20 min to render the surface hydrophilic. Dome-like nanostructures were fabricated using PS particles with diameters of 200, 500, 1000, and 3000 nm as a sacrificial template (5.0 % w/v, SPHERO™ Polystyrene Particles, Spherotech). For the Langmuir–Blodgett method, the PS template solution was concentrated to 10 wt% and mixed with ethanol in a 1:1 ratio. The PS template monolayer was transferred onto the Pt-IDE-patterned SiO_2/Si substrates after pipetting the mixed solution onto a glass slide positioned at an angle of 45° in a Petri dish containing deionized water. All samples were placed in a dry box to remove the template solution for 24 hours. After forming monolayered PS templates (0.3, 0.5, 1, 3 μm), all samples were loaded into an electron beam evaporator (Korea Vacuum) for the deposition of 150 nm-thick In_2O_3 (99.99 %, Taewon Scientific Co.) film. Evaporation was carried out at a glancing angle (15°) with a rotation speed of 3 rpm and base pressure and growth rate were 1×10^{-6} Torr and 1 Å/s respectively. Also, plain In_2O_3 film was deposited on the substrate without a PS template to compare the structural effects. All samples were annealed with ambient air at 500 °C in a box furnace for 1 h to remove the PS templates and simultaneously crystallize the In_2O_3 film, resulting in In_2O_3 HHs. To decorate Au NPs on the entire surface of In_2O_3 HHs, a 3-nm-thick Au film (99.99 %, Taewon Scientific Co.), reported as the optimal thickness in our previous work, was deposited on the substrate at the original position (0°) with evaporation of 0.1 Å /sec and a rotation speed of 0 rpm [43]. Then, the Au film-deposited In_2O_3 HHs were placed again in a box furnace (500 °C, 1 hour) to change Au film into Au NPs, leading to In_2O_3 HHs with Au NPs.

2.2. Characterization

The samples' top-view and cross-sectional morphologies were analyzed using field-emission scanning electron microscopy (FE-SEM; JSM-7610F-Plus, JEOL). Further detailed cross-sectional morphology was examined using an acceleration voltage of 15 kV and a working distance of 8 mm. Additional crystallographic information was acquired using X-ray diffraction (XRD; Empyrean, PANalytical) with Cu-Kα irradiation (λ=1.5418 Å), a tube voltage of 40 kV, and a current of 30 mA. The surface composition and chemical states of sensing materials were analyzed using X-ray photoelectron spectroscopy (XPS; AXIS SUPRA, KRATOS) with monochromated Al Kα (survey analysis with 160 eV and high-resolution analysis with 20 eV).

2.3. Gas-sensing measurements

The gas sensor measurement system comprised a mini probe chamber outfitted with a 12-channel probe system (MPS6000, PHOCOS), along with a gas controller (PHOCOS) capable of precisely adjusting the gas concentration between 1 and 50 ppm and a temperature controller (PHOCOS). The dimensions of the sensing chamber were 140 mm (width) × 80 mm (length) × 40 mm (height). The gas was injected in a repeating sequence of dry air and target gas (CH_4, CH_3COCH_3, $CH_3CH_2CH_3$, C_2H_5OH, H_2, and C_5H_8 (all balanced with dry air, RIGAS) through an automated gas controller control system. The operating temperature was controlled by a silicon nitride type heater at 150 °C, 200 °C, 250 °C, 300 °C, 350 °C and 400 °C to evaluate the gas response mechanism at different operating temperatures. The response to the target gas was measured at a DC bias constant voltage of 0.1 V using a

source meter (Keithley 238, KEITHLEY), and a high-density switch system (7001 switch system, KEITHLEY) accurately measured the sensor resistance. The resistance variation was measured at 1-second intervals using I.V. Solution's software program to analyze the gas response.

2.4. Theoretical detection limit calculations

The detection limit for C_5H_8 was derived from the signal processing performance of the sensor. Before exposure to C_5H_8, ten consecutive points were recorded at baseline. Then, a fifth-order polynomial fit was applied over the data range to obtain a curve-fitting equation and statistical parameters of the polynomial fit.

$$Vx^2 = \sum (y_i - y)^2 \tag{1}$$

where y_i represents the measured data point and y denotes the corresponding value derived from the curve-fitting equation. The root-mean-square (rms) noise was calculated as follows:

$$rmsnoise = \sqrt{\frac{Vx^2}{N}} \tag{2}$$

where N denotes the number of data points employed in the curve-fitting process. The theoretical detection limit (DL) was calculated using the following equation:

$$DL(ppm) = 3\left(\frac{rms}{slope}\right) \tag{3}$$

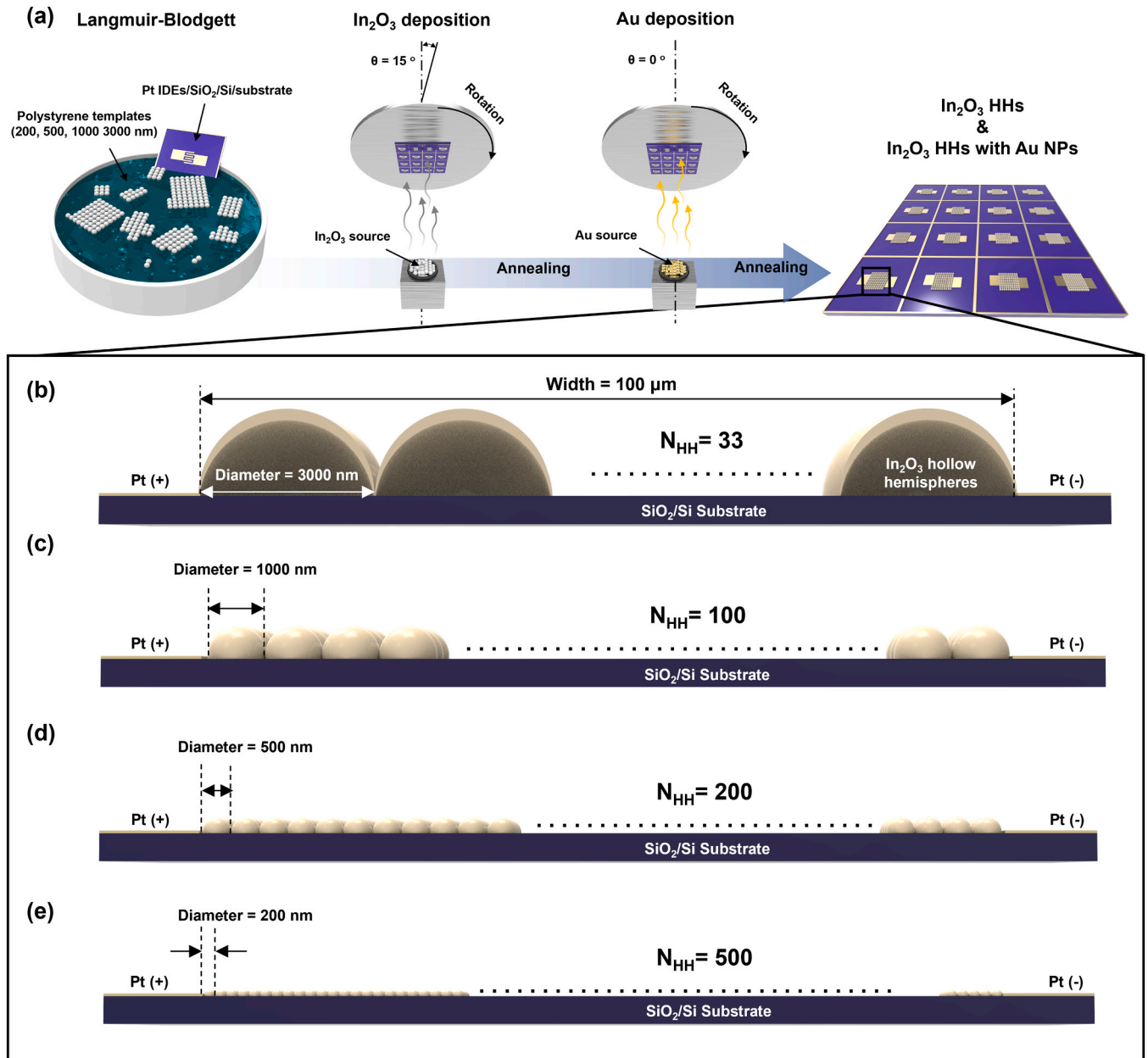Further elaboration of the calculation of the theoretical DL can be found in a previous report [5].

Fig. 1. (a) Schematic illustrations of fabrication procedure for high-performance gas sensor based on highly ordered In_2O_3 HHs with Au NPs. Schematic illustrations of the number of In_2O_3 HHs monolayer formed between the electrodes with a spacing of 100 μm as a function of diameters of In_2O_3 HHs: (b) 3000 nm (c) 1000 nm, (d) 500 nm, and (e) 200 nm.

3. Results and Discussion

3.1. Design concept of In₂O₃ HHs sensor

In general, the gas-sensing properties of metal oxide-based gas sensors are influenced by three fundamental factors: the transducer function, utility factor, and receptor function [44–46]. The transducer function enables the conversion of electrical signals caused by chemical adsorption on the oxide surface into electrical signals, whereas the utility factor is related to the access of the target gas to the inner oxide grains. Notably, nanostructured gas sensors fabricated using PS templates exhibit significantly improved transducer function and utility factors, which are closely related to the size of the PS template particles [25]. To determine the optimal size of the PS template particles for high-performance gas sensors, we fabricated nanostructured gas sensors with various PS templates, with particle sizes of 200–3000 nm. A schematic illustration of the fabrication procedure is presented in Fig. 1a. A PS monolayer with a hexagonal close packing was first formed on Ultraviolet-Ozone (UVO)-treated substrates with Pt IDEs using the Langmuir–Blodgett method. Subsequently, In₂O₃ and Au were sequentially deposited on the PS monolayer by e-beam evaporation. When the PS templates were burned out during the annealing process, In₂O₃ crystallized, and the Au film agglomerated into Au nanoparticles. Fig. 1b-e show the number of In₂O₃ HHs that can be formed between Pt electrodes with a spacing of 100 μm. Utilizing PS template particles of

3000 nm in size resulted in the formation of approximately 33 In₂O₃ HHs. When employing PS template sizes of 1000, 500, and 200 nm, approximately 100, 200, and 500 In₂O₃ HHs could be formed between the Pt electrodes.

3.2. Structural and morphological characteristics

Fig. 2a-j illustrate the top-view and cross-sectional SEM images of monolayered In₂O₃ HHs fabricated using the PS template particles of various sizes. The thin In₂O₃ shell (150 nm in thickness) was evident in the images. A flat film was used as a reference. After annealing process, PS templates were completely removed and both the height and diameter of all In₂O₃ HHs became larger than those of PS templates. These nanodome-shaped In₂O₃ HHs formed a monolayer with contact between the adjacent nanodomes, forming highly ordered hexagonal close-packed structures. We investigated the surface functionalization process, transitioning from bare In₂O₃ HHs to In₂O₃ HHs adorned with Au NPs, was investigated (Fig. 2k-n). To optimize the C₅H₈ sensing properties, we controlled the amount and size of Au NPs through E-beam and furnace treatments. The deposited Au NPs, measuring 35–50 nm, completely covered the surfaces of the In₂O₃ HHs. Fig. 2k shows that the diameter and distribution of Au NPs were bigger and rougher toward the center, in contrast, smaller and denser toward the bottom part due to hemispherical shape of In₂O₃ HHs. The deposited Au NPs (35–50 nm), exhibited complete coverage on the surface of In₂O₃ HHs, as shown in
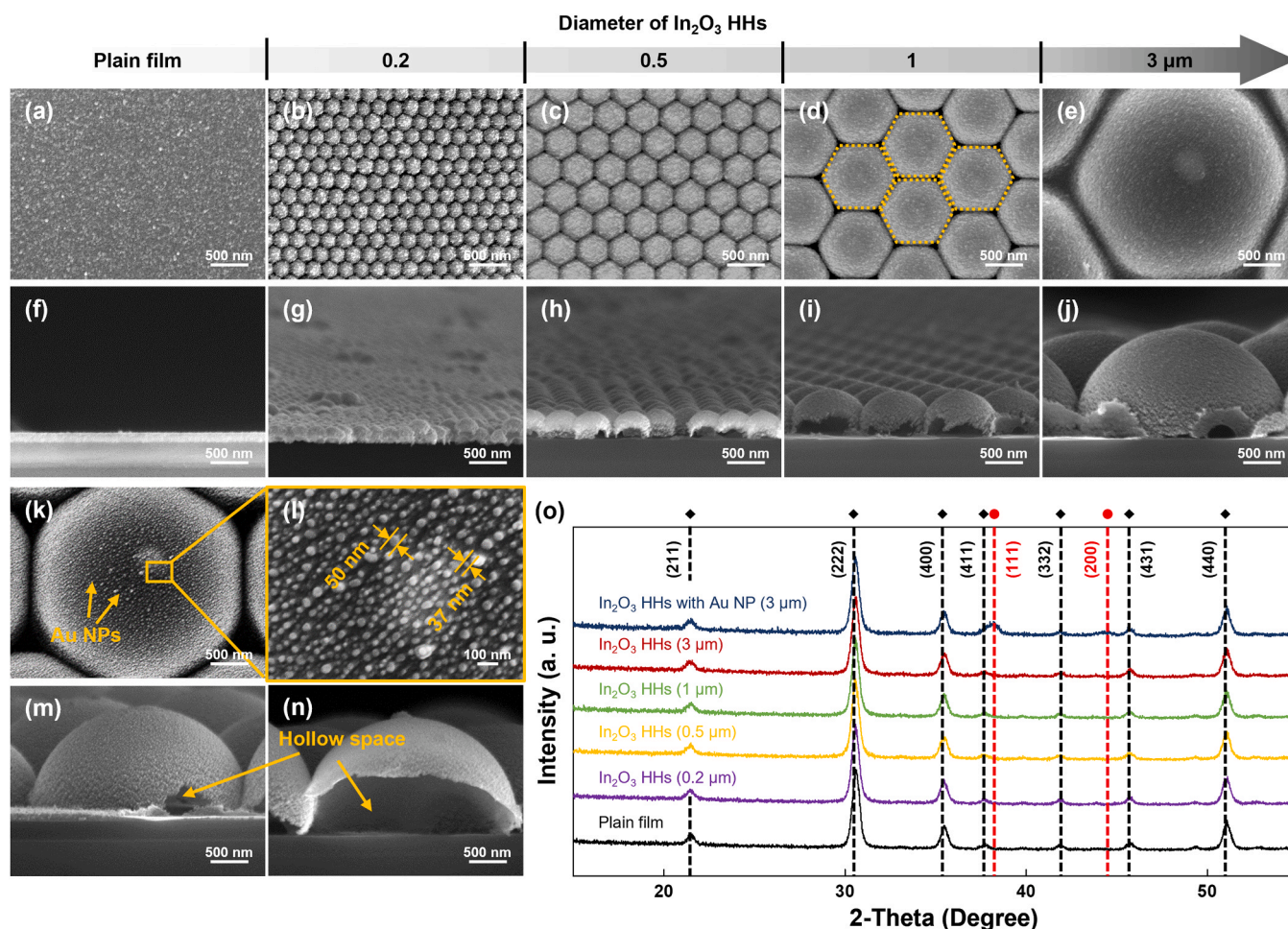

Fig. 2. Plain-view SEM micrographs of (a) plain film without PS template templates and (b-e) In₂O₃ HHs fabricated using PS templates with diameters of 200 nm, 500 nm, 1000 nm, and 3000 nm, respectively; the yellow line in (d) showing the periodicity of the In₂O₃ HHs. (f-j) Cross-sectional SEM micrographs showing the thickness of the In₂O₃ HHs increasing with the diameter. (k) Plain-view and (m) cross-sectional SEM micrographs of In₂O₃ HHs with Au NPs. (l) High magnification SEM image of the selected area in (k). SEM micrograph of (n) showing inner side of the In₂O₃ HHs with Au NPs. (o) XRD patterns of In₂O₃ HHs with various diameters and In2O3 HHs with Au NPs.

Fig. 2l. From the Fig. 2**m and 2n**, it is clearly reaffirmed that PS template has been completely removed during annealing process, revealing a hollow structure. The crystallinity of the In_2O_3 HHs, both before and after Au NP decoration, was examined using XRD (Fig. 2**o**). Irrespective of the PS template size, the presence of multiple XRD peaks indicates the polycrystalline nature of the In_2O_3 HHs, which is consistent with the body-centered cubic phase of In_2O_3 (ICDD 01–071–2194). Furthermore, the representative peaks for the (111) and (200) planes of Au (JCPS 04–0784) were discernible after Au decoration, suggesting that Au was uniformly deposited on the surface without stacking. We conducted an XPS analysis to confirm any interaction between Au and In_2O_3 HHs, as shown in Fig. S1. The peaks at approximately 83.5 and 87.2 eV are attributed to $Au4f_{7/2}$ and $Au4f_{5/2}$ (see Fig. S1 (a)), while the two peaks located at 444.2 and 451.7 eV are assigned as $In3d_{5/2}$ and $In3d_{3/2}$ (see Fig. S1 (b)), respectively. These results indicated there is no interaction between Au NPs and In_2O_3 HHs and they are consistent with previous reports [47,48]. Fig. S1 (c) shows the O1s core level spectrum, which was deconvoluted using the Gaussian method to three peaks at 529.7 eV, 530.7 eV, and 531.3 eV, designated as lattice oxygen, oxygen vacancy, and chemisorbed oxygen species [49].

3.3. Gas sensing properties of In_2O_3 HHs

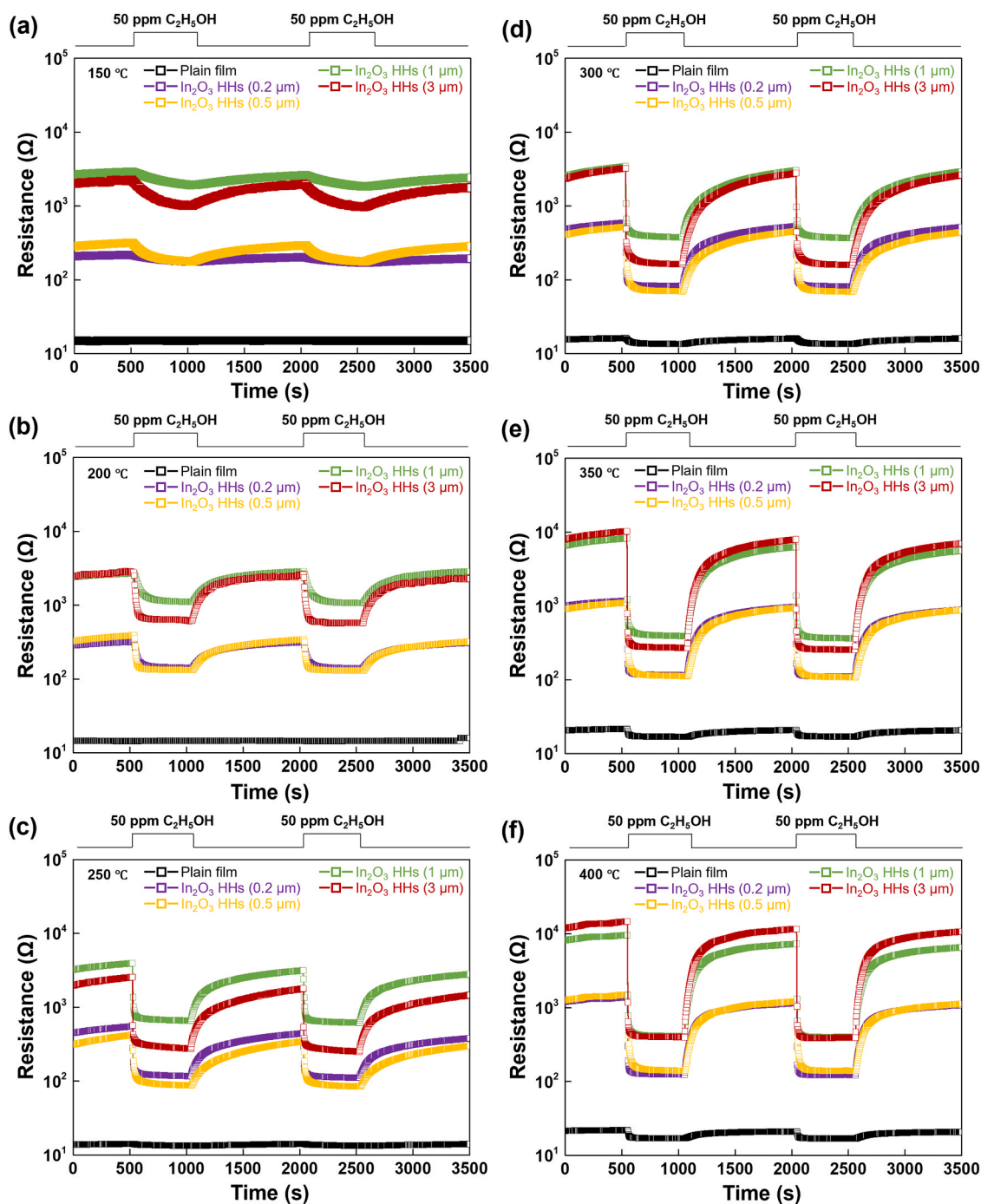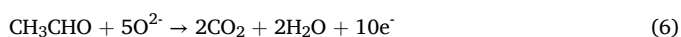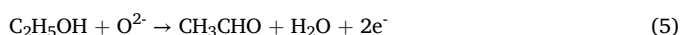The operational principle of metal-oxide gas sensors relies on the

Fig. 3. Resistance curves for 50 ppm C_2H_5OH as a function of diameter of In_2O_3 HHs at different temperature; (a) 150 °C, (b) 200 °C, (c) 250 °C, (d) 300 °C, (e) 350 °C, (f) 400 °C.

modulation of an electron-depletion layer [50]. In n-type metal oxides, such as In_2O_3, atmospheric oxygen is adsorbed on the metal-oxide surface, forming ion states by extracting electrons from the metal oxide [40, 51]. This results in the development of an initial electron-depletion layer on the metal-oxide surface. Depending on the nature of the target gas, it either reacts with surface oxygen ions to release electrons to the metal oxide (in the case of a reducing gas), or extracts electrons from the metal oxide (in the case of an oxidizing gas). These interactions lead to changes in the width of the electron-depletion layer. The gas response was quantified by comparing the electrical resistance of the gas sensor under an airflow (R_a) with that of the sensor under a target gas (R_g). As a representative reducing gas, C_2H_5OH (ethanol) gas releases electrons to metal oxides and is adsorbed onto the surface, thereby reducing the electrical resistance of the sensor. Consequently, the gas response (S) is expressed as (R_a/R_g-1). The response to C_2H_5OH gas is intricately linked to the number of oxygen ions adsorbed onto the metal oxide. With increasing operating temperature, the amount of oxygen ions (O_2^-, O^-, and O^{2-}) adsorbed on the surface of the In_2O_3 HHs results in a baseline resistance (Fig. S2). Additionally, C_2H_5OH adsorption becomes more active because of the increased thermal energy, leading to an improved gas response. The proposed gas reaction pathways for the oxygen ions and C_2H_5OH gas are summarized as follows:

$$1/2O_2(g) + e^- = O^-(ad) \tag{4}$$

$$C_2H_5OH + O^{2-} \rightarrow CH_3CHO + H_2O + 2e^- \tag{5}$$

$$CH_3CHO + 5O^{2-} \rightarrow 2CO_2 + 2H_2O + 10e^- \tag{6}$$

To optimize the geometric factor based on the gas-sensing mechanism and temperature simultaneously, we measured the response of pristine In_2O_3 HHs (with different HH diameters) to 50 parts per million (ppm) of C_2H_5OH at operating temperatures of 150– 400 °C (Fig. 3a-f). The thin-film In_2O_3 at 150 °C exhibited negligible gas response due to a limited active surface area for chemical reactions with C_2H_5OH (Fig. 3a). In contrast, the In_2O_3 HHs demonstrated gas detection by reducing the resistance upon gas exposure, showing substantial resistance changes. The sensors with larger In_2O_3 HH diameters showed improved responses, which is attributed to the higher surface area within the given monolayer structure. The In_2O_3 HHs with diameters of 3000 nm were identified as the optimal size for the sensor. As the measurement temperature increases, particularly from 200 to 400 °C, the gas responses of all samples to C_2H_5OH became faster. In particular, the 3-μm In_2O_3 HH sensor immediately reacted upon gas injection with an extremely fast response time (<3 s) and full recovery in approximately 1000 s. In our experiments, the gas response at 350 °C was the most stable and reproducible, demonstrated by the sharpest gas-dependent transient curves.

Fig. 4 summarizes the calculated responses and response times to 50 ppm C_2H_5OH reconstructed from the measurements in Fig. 3, to highlight the operating-temperature dependence of the sensors with various diameters of In_2O_3 HHs. The overall sensor responses were enhanced by increasing both the diameter of the In_2O_3 HHs and operating temperature (Fig. S3). Notably, sensors with 3-μm In_2O_3 HHs operated at 350 °C exhibited a 132-fold enhancement in response to 50 ppm C_2H_5OH compared to the thin-film control, highlighting the optimized experimental parameters of the sensor achieved in this work.

3.4. Selectivity of In_2O_3 HHs with Au NPs

Fig. 5 illustrates the sensor responses at 350 °C to various pollutant gases (50 ppm CH_4, C_3H_8, H_2, CH_3COCH_3, C_2H_5OH, and C_5H_8) to assess the selectivity of In_2O_3 HH-based sensors (with the HH diameter fixed to the optimal diameter of 3 μm), both before and after decoration with Au NPs (the resistance data is presented in Fig. S4). The sensor comprising In_2O_3 HHs with Au NPs exhibited an overall enhanced response to various 50 ppm gases compared to that comprising bare In_2O_3 HHs.
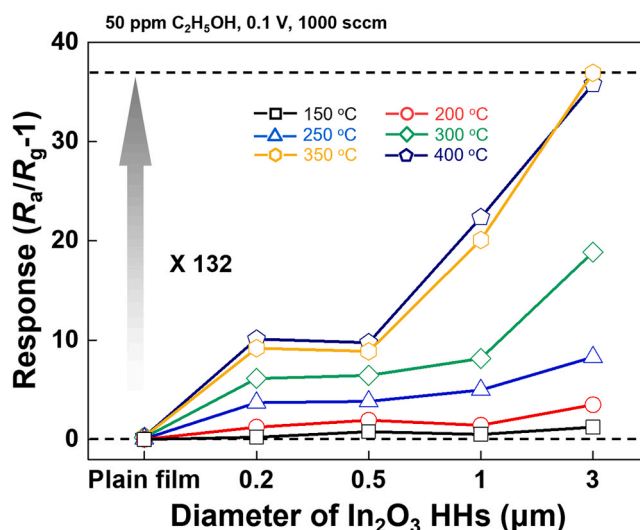

Fig. 4. Gas responses for plain film and highly ordered In_2O_3 HHs based gas sensors as a function of diameter of In_2O_3 HHs.

Specifically, the gas sensors displayed low responses to CH_4, C_3H_8, and H_2 because of their relatively inert nature and the lack of specific interaction pathways with the surface of In_2O_3 HHs with Au NPs. However, the sensors exhibit relatively high responses to CH_3COCH_3 and C_2H_5OH, and the In_2O_3 HHs with Au NPs showed the highest response to C_5H_8, interestingly. These results can be attributed to catalytic effects, such as the electronic and chemical sensitization by Au NPs [25,52], which enhances the depletion region changes and interactions between gas molecules and the sensor surface. In particular, C_5H_8 in exhaled breath has been linked to several health conditions and diseases such as diabetes [53], liver cirrhosis [54], and liver cancer [55]. Those disease biomarker in exhaled breath, can be effectively detected by sensors based on In_2O_3 HHs with Au NPs, showing a significant improvement in gas responses compared with the bare In_2O_3 HHs sensor. To precisely analyze the effect of Au decoration on the gas-sensing properties, the responses and the increase ratio of the response with response times ($t_{90\%}$(air-to-gas)) to 50 ppm CH_4, C_3H_8, H_2, CH_3COCH_3, C_2H_5OH, and C_5H_8 are plotted in Fig. 6. The increase ratio is defined as S_b/S_a, where S_a and S_b are the responses of the bare In_2O_3 HHs and In_2O_3 HHs with Au NPs, respectively. The sensors based on pristine In_2O_3 HHs exhibited some response to C_2H_5OH, but with the poor selectivity typical of SMO materials (Fig. 6a). In contrast, the major response of the In_2O_3 HHs to C_5H_8 completely changed after decoration with Au NPs (Fig. 6b). The responses to CH_3COCH_3 and C_2H_5OH were notably diminished after Au decoration, whereas the response to C_5H_8 was enhanced. The S_b/S_a between sensors based on In_2O_3 HHs and In_2O_3 HHs with Au NPs are shown in Fig. 6c, which highlights the critical impact of Au catalyst decoration on metal oxides for highly selective detection. Among the various gases, the In_2O_3 HHs with Au NPs exhibited the highest S_b/S_a of 31.7 for C_5H_8. To clarify the electronic and chemical sensitizations provided by the decoration of In_2O_3 HHs with Au NPs, the $t_{90\%}$(air-to-gas) values for 50 ppm CH_4, C_3H_8, H_2, CH_3COCH_3, C_2H_5OH, and C_5H_8 are summarized in Fig. 6d. For C_3H_8 and H_2, the In_2O_3 HHs with Au NPs showed response times of 6 and 11 s, respectively, whereas the In_2O_3 HHs without Au NPs showed response times of 5 and 9 s, respectively, indicating an increase in the response times after Au NP functionalization. In contrast, for CH_4, CH_3COCH_3, C_2H_5OH, and C_5H_8, the In_2O_3 HH-based sensors with Au NPs showed response times of 7, 5, 3, and 2 s, respectively, indicating faster responses than that without Au NPs (Fig. 6d). In particular, for C_5H_8, the response time decreased significantly from 10 to 2 s after the Au NPs decoration (Fig. 6e). Based on the results shown in Fig. 6, the important findings are summarized as follows: (i) the In_2O_3 HHs with Au NPs show an
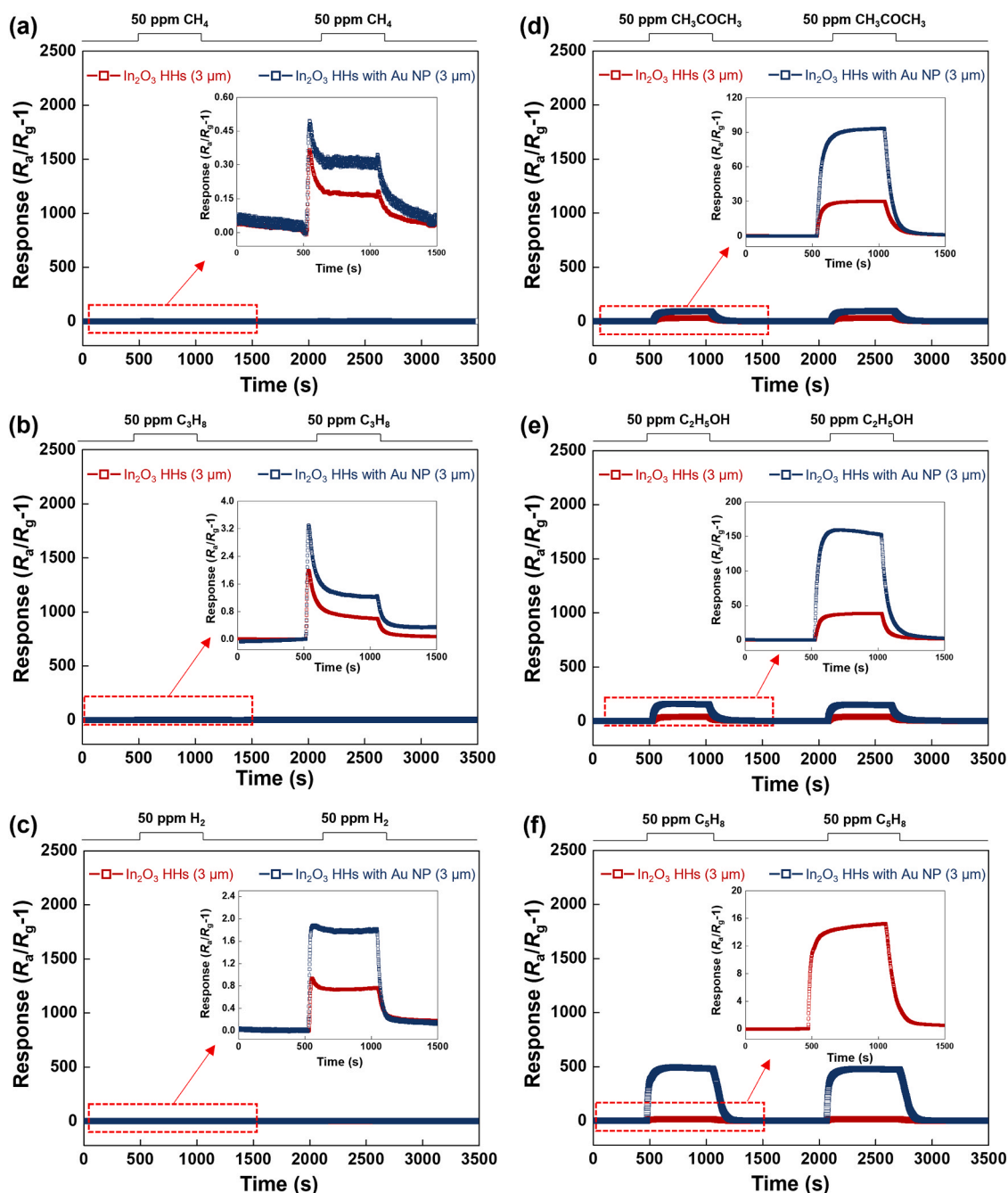
Fig. 5. Response curves of the In$_2$O$_3$ HHs with and without Au NPs to 50 ppm various gases at 350 °C; (a) CH$_4$, (b) C$_3$H$_8$, (c) H$_2$, (d) CH$_3$COCH$_3$, (e) C$_2$H$_5$OH, (f) C$_5$H$_8$ and (g) HCHO. The insets show the magnified response curves in selected areas.

extremely high response ($S = 483$) and the highest S_b/S_a (31.7) value to C$_5$H$_8$; (ii) a high porosity enables effective gas diffusion, which enhances the reaction between the gas molecules and sensing materials; (iii) Au NPs on the In$_2$O$_3$ HHs provide electronic sensitization under C$_3$H$_8$ and H$_2$ atmospheres, resulting in an increase in the response and response times; (iv) Au NPs on the In$_2$O$_3$ HHs provide both electronic and chemical sensitization in the presence of CH$_4$, CH$_3$COCH$_3$, C$_2$H$_5$OH, and C$_5$H$_8$, resulting in a decrease in the response times and an increase in the response values. Hence, Au decoration of the highly sensitive and selective C$_5$H$_8$ gas sensor developed in this work enhances the gas-sensing performance through both electronic and chemical sensitization. The detailed operating mechanism is elaborated in the subsequent section.

In comparison to previously reported gas sensors for C$_5$H$_8$ detection, the fabricated In$_2$O$_3$ HHs functionalized with Au NPs exhibits superior

sensing capabilities, such as the response and response time (Fig. 7). It is clear that the results achieved in this study are competitive, especially for ppm-level detection. In the context of Internet of Everything applications, the remarkably sensitive and selective gas-sensing capabilities across a broad concentration range can play a pivotal role in advancing the development of indoor environmental monitoring systems, as well as disease diagnosis devices that collect disease biomarkers from exhaled breath [56].

To further validate the gas-sensing characteristics, including the stability and detection limit, of In$_2$O$_3$ HHs with and without Au NPs, the sensors were exposed to multiple pulses of C$_5$H$_8$ at varying concentrations. As the gas concentration increased, the response of the sensor increased. The sensors based on In$_2$O$_3$ HHs exhibited response values of 1.3, 2.2, 2.7, and 3.9–1, 2, 3, and 4 ppm C$_5$H$_8$, respectively, while those
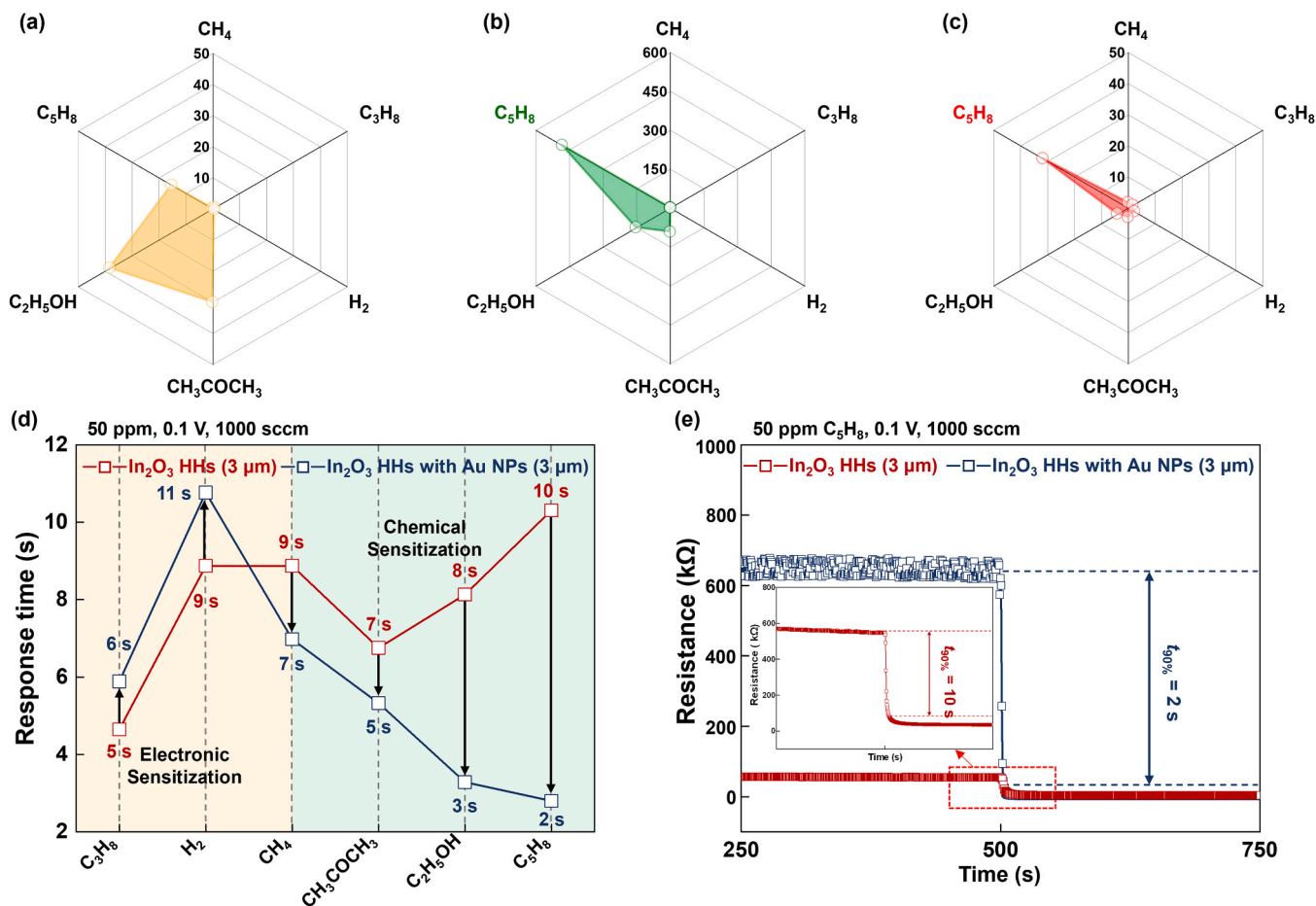
Fig. 6. Polar plot of responses of (a) In_2O_3 HHs and (b) In_2O_3 HHs with Au NPs to 50 ppm CH_4, C_3H_8, H_2, CH_3COCH_3, C_2H_5OH, and C_5H_8. (c) The response ratios (S_b/S_a) between In_2O_3 HHs and In_2O_3 HHs with Au NPs. S_a and S_b represent the gas responses of In_2O_3 HHs and In_2O_3 HHs with Au NPs, respectively. (d) Enhanced electronic and chemical sensitizations were achieved by decorating In_2O_3 HHs with Au NPs. (e) Response time ($t_{90\%}$) of In_2O_3 HHs and In_2O_3 HHs with Au NPs.
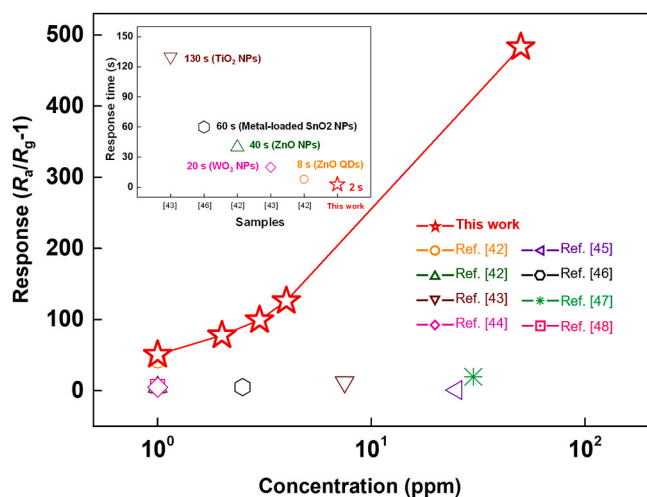

Fig. 7. Responses toward the detection of C_5H_8 reported in literature.

based on In_2O_3 HHs with Au NPs gave values of 68, 93, 109, and 122, respectively. The gas responses of In_2O_3 HH-based sensors demonstrated a linear correlation with gas concentration (slope = 0.8 ppm^{-1}), as illustrated in Fig. 8a. Although the lowest concentration of C_5H_8 evaluated in this study was 1 ppm, a theoretical DL as low as 1 ppb (parts per billion) was calculated by extrapolating the linear relationship to the point where the signal-to-noise ratio was 3. Furthermore, this

performance was significantly improved by incorporating Au NPs, as highlighted by a good linearity (slope = 17.8 ppm^{-1}) and detection limit of 743 ppt (Fig. 8b). The response times of the sensors based on In_2O_3 HHs and In_2O_3 HHs with Au NPs as a function of the C_5H_8 concentration are shown in Fig. 8c,d. As the concentration of C_5H_8 decreased, the response increased, demonstrating a fast response even at extremely low concentrations, with a response time of 15 s for 1 ppm C_5H_8. In order to utilize the sensor for the breath analyzer, it is essential to ensure its performance with stability in a humid environment. When In_2O_3 HHs with Au NPs repeatedly exposed to different concentrations of C_5H_8 from 3 to 10 ppm at optimal temperature in R.H. 80 %, they exhibit excellent stability without degradation and theoretical detection limits (signal-to-noise ratio > 3) are calculated to be extremely low as 43 ppb for C_5H_8, as shown in Fig. S5. Such an ultrahigh response with a fast response time offers additional potential for detecting extremely low concentrations of target gases, including those associated with explosives and narcotics.

3.5. Size effect of In_2O_3 HHs and role of Au NPs on the surface

To interpret the superior response and selectivity of In_2O_3 HHs with Au NPs to C_5H_8, the transducer function, utility factor, and receptor function were considered as fundamental parameters. Fig. 9a shows the mechanism underlying the response enhancement by optimizing the size of the PS template particles. As mentioned earlier, the gas response is defined by the ratio of the baseline resistance in the air to the resistance when the target gas is adsorbed, meaning that a high response can be achieved by maximizing the change in total resistance ($R_T = R_c + \Sigma$
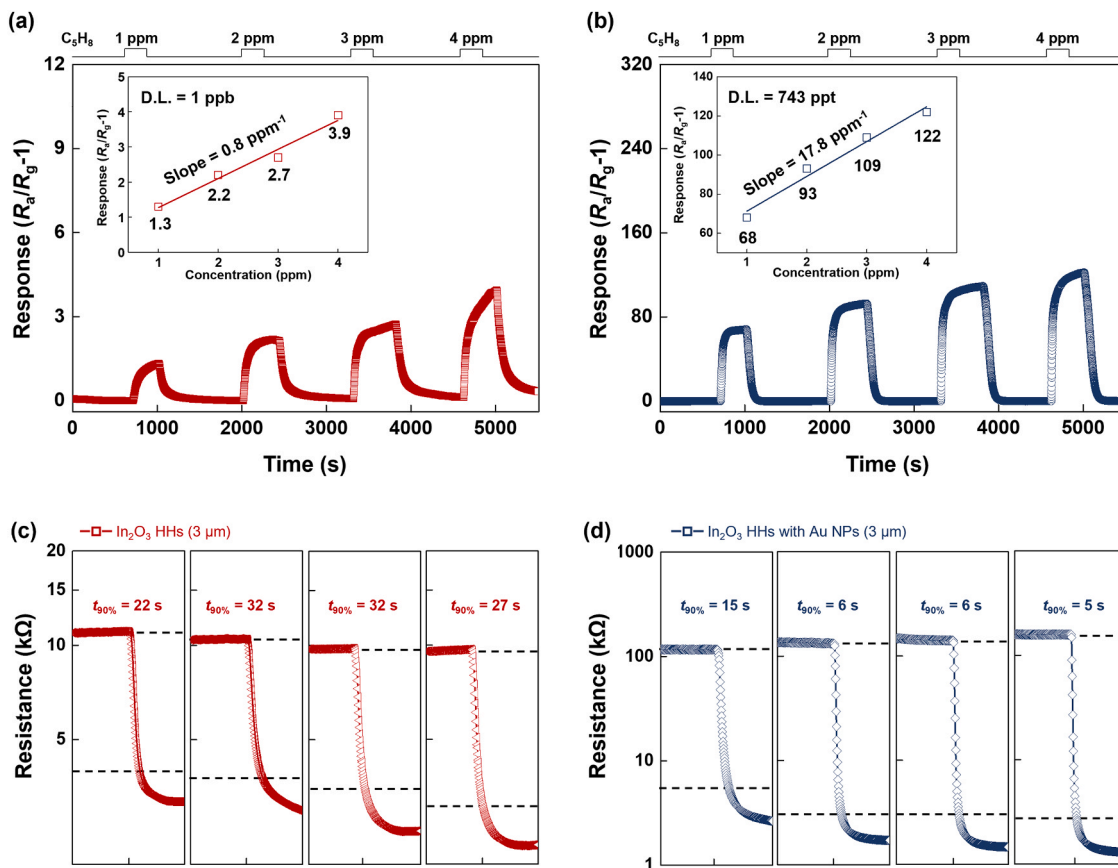
Fig. 8. Sensing curves of (a) In$_2$O$_3$ HHs and (b) In$_2$O$_3$ HHs with Au NP toward 1, 2, 3 and 4 ppm C$_5$H$_8$. (inset: responses of the In$_2$O$_3$HHs as a function of C$_5$H$_8$ concentration.) (c) Sensing curves of In$_2$O$_3$ HHs toward 1, 2, 3, and 4 ppm C$_5$H$_8$. (d) Sensing curves of In$_2$O$_3$ HHs with Au NPs toward 1, 2, 3, and 4 ppm C$_5$H$_8$.
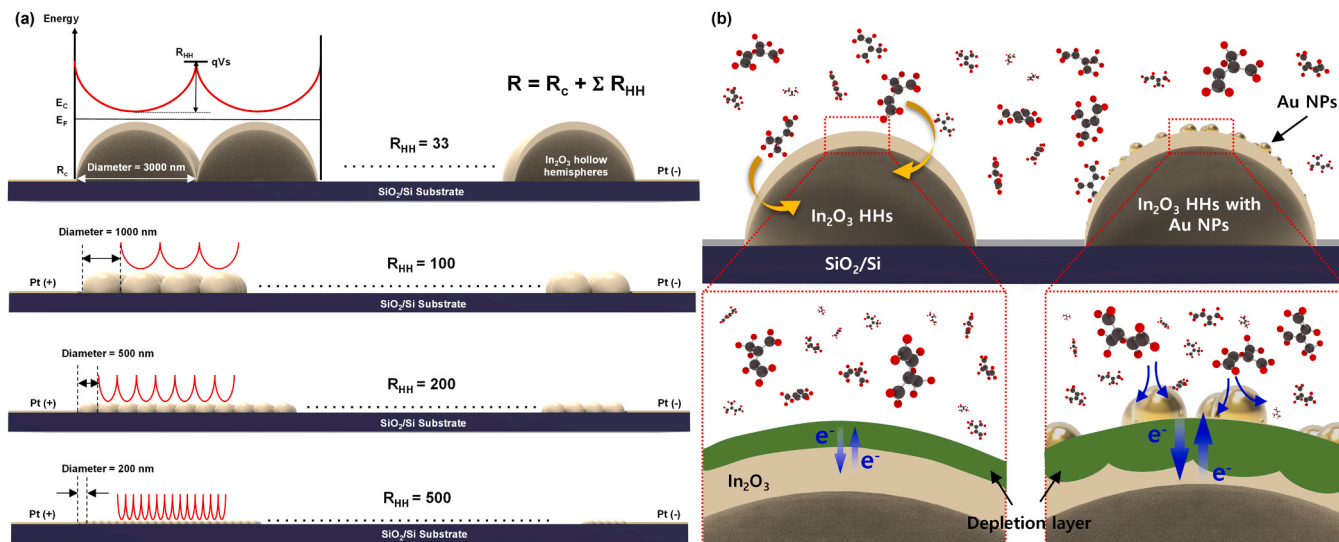

Fig. 9. (a) Schematic illustration of In$_2$O$_3$ HHs sensing layer with energy bands, which shows the number of double Schottky barrier between In$_2$O$_3$ HHs. (b) Schematic illustration for C$_5$H$_8$ adsorption on In$_2$O$_3$ HHs with Au NPs. Note that the width of the surface depletion region is drastically increased by Au NPs via electronic and chemical sensitizations.

R_{HH}). The R_T of gas sensors based on nanostructured materials is significantly influenced by the double Schottky barriers formed between adjacent nanostructures [6]. A high response can be achieved by modulating and increasing the number of double Schottky barriers. Given the IDEs electrode design (100-μm gap), the number of interfaces between the PS template particles in the monolayer was assumed to

equal the number of barriers for simplicity. Therefore, approximately 500, 200, 100, and 33 double-Schottky barriers can be formed for In$_2$O$_3$ HHs formed using PS template particles with sizes of 200, 500, 1000, and 3000 nm, respectively. Although the In$_2$O$_3$ HHs formed using 200-nm PS particles resulted in the most double Schottky barriers in the nanostructures, they showed the lowest response. In contrast, the

highest response was observed for the In_2O_3 HHs prepared using the 3,000-nm PS particles (with the fewest double Schottky barriers), followed by those prepared using the 1,000- and 500-nm PS templates. Therefore, it is assumed that there are stronger influencing factors than the number of double Schottky junctions in terms of the gas response. To identify these factors, we simplified the surface area of the In_2O_3 HHs as $A_I=2\pi r^2$, where r is the radius of the PS template particles. As the radius of the In_2O_3 HHs increases to approximately 100, 250, 500, and 1500 nm, the total surface areas (TA_I) of In_2O_3 HHs corresponding to the lengths are 31415900, 78539750, 157079500, and 466526115 nm^2, respectively. Assuming a monolayer, a particle diameter of 3000 nm yields a TA_I that is approximately 15 times larger than that of the 200-nm case. Considering that the number of double Schottky junctions for the sensor fabricated with 200-nm PS particles is nearly 15 times higher than that for the 3,000-nm case, it is obvious that A plays a more critical role in determining the chemoresistive response. It is noteworthy that the larger volume of double Schottky junctions for In_2O_3 HHs with higher A offers an additional effect owing to the intrinsic polycrystallinity of In_2O_3. It should also be considered that when the size of the PS template is less than the In_2O_3 deposition thickness, the effect on the surface is greater than that of the double Schottky barrier.

The role of the Au NPs in the electronic and chemical sensitizations of In_2O_3 for C_5H_8 sensing is illustrated in Fig. 9**b.** The Au NPs on the surface of the In_2O_3 HHs create Schottky junctions and extract electrons from In_2O_3, thereby increasing the widths of the interfacial electron depletion regions, which is consistent with the increase in the base resistance (Fig. S2). Additionally, As seen in Fig. S6, α indicates the angle from the center point of In_2O_3 HHs to the points of contact with adjacent HHs. An increase in the α means that the thickness of the contact area between adjacent In_2O_3 HHs increases. For these reasons, the height of the potential barrier of each In_2O_3 HHs changes. Accordingly, the In_2O_3 HHs using the 3000 nm-sized PS template consequently exhibit the highest base resistance, while those using the 200 nm-sized PS template exhibit the lowest base resistance. When the PS template size increases to 1 micrometer, it can be considered that a complete electron depletion layer (EDL) forms, resulting in a significant increase in base resistance and gas response as shown in Fig. 3. Thus, the In_2O_3 HHs with Au NPs exhibited more efficient resistance modulation upon exposure to C_5H_8. In previous studies, Lee et al. reported the mechanism and chemical reactions of Au-catalyst-based gas sensors selectively detecting C_5H_8 using a real-time proton-transfer-reaction mass spectrometer (PTR-QMS) [57]. When C_5H_8 was exposed to Au-catalyst-based materials, various intermediate compounds were generated, with acetaldehyde signals concentrations being notably high. Acetaldehyde is a gas well-known for indicating a high response when detected, so the reforming of C_5H_8 by Au NPs to produce acetaldehyde significantly enhances the C_5H_8 gas sensing properties. This phenomenon is also experimentally observed in In_2O_3 HHs with Au NPs, where the selectivity is increased through the interaction between Au and C_5H_8 at elevated temperatures. Additionally, the remarkably rapid response time exhibited by In_2O_3 HHs functionalized with Au NPs (<2 s) demonstrates the excellent C_5H_8 dissociation effect provided by the Au NPs. In addition, sensors comprised of In_2O_3 HHs with Au NPs based on 3,000-nm PS templates, which have larger pores than the other sensors based on smaller PS templates, facilitated gas diffusion, which further reduced the response time. These results highlight the potential of Au NPs as reliable catalysts for high-performance C_5H_8 sensing using In_2O_3 HHs.

4. Conclusions

This study focused on the contribution of the size effect of PS template particles on the resulting gas-sensing performance of sensors based on In_2O_3 HHs. The sensor fabricated using the largest template particles showed better overall performance for C_5H_8 detection compared to those based on smaller particles. This observation has a significant impact on chemoresistor applications, where the effect of the surface area dominates that of the double Schottky barrier for monolayer sensors. The decoration of Au NPs on n-type semiconductors further amplified their response and selectivity towards C_5H_8. These sensors are expected to be suitable for detecting biomarkers associated with various diseases in exhaled breath. These findings provide a deeper understanding of the key factors determining the gas-sensing performance and new insights into gas-sensor technology based on template methods.

CRediT authorship contribution statement

Yun-Haeng Cho: Resources, Methodology. **Young-Seok Shim:** Investigation, Data curation. **See-Hyung Park:** Writing – original draft, Investigation, Data curation. **Jae Han Chung:** Methodology, Investigation. **Sungwoo Sohn:** Investigation, Data curation. **Donghwi Cho:** Writing – review & editing, Supervision, Conceptualization. **Gye Hyeon Lee:** Methodology, Investigation. **Junho Hwang:** Writing – original draft, Investigation, Data curation. **Wooyoung Lee:** Writing – review & editing, Supervision, Conceptualization. **Kwangjae Lee:** Writing – review & editing, Supervision, Conceptualization. **Myungwoo Choi:** Resources, Methodology. **Jinho Lee:** Methodology, Investigation.

Declaration of Competing Interest

The authors declare the following financial interests/personal relationships which may be considered as potential competing interests: Wooyoung Lee reports financial support was provided by Yonsei University. Young-Seok Shim reports financial support was provided by Korea University of Technology & Education. If there are other authors, they declare that they have no known competing financial interests or personal relationships that could have appeared to influence the work reported in this paper.

Data Availability

Data will be made available on request.

Appendix A. Supporting information

Supplementary data associated with this article can be found in the online version at doi:10.1016/j.snb.2024.136500.

References

[1] N. Baig, I. Kammakakam, W. Falath, Nanomaterials: a review of synthesis methods, properties, recent progress, and challenges, Mater. Adv. 2 (2021) 1821–1871.

[2] S. Su, W. Wu, J. Gao, J. Lu, C. Fan, Nanomaterials-based sensors for applications in environmental monitoring, J. Mater. Chem. 22 (2012) 18101–18110.

[3] Z. Meng, R.M. Stolz, L. Mendecki, K.A. Mirica, Electrically-transduced chemical sensors based on two-dimensional nanomaterials, Chem. Rev. 119 (2019) 478–598.

[4] D. Cho, J.M. Suh, S.H. Nam, S.Y. Park, M. Park, T.H. Lee, et al., Optically activated 3D thin-shell TiO2 for super-sensitive chemoresistive responses: toward visible light activation, Adv. Sci. 8 (2021) 2001883.

[5] D. Cho, Y.S. Shim, J.W. Jung, S.H. Nam, S. Min, S.E. Lee, et al., High-contrast optical modulation from strain-induced nanogaps at 3D heterogeneous interfaces, Adv. Sci. 7 (2020) 1903708.

[6] J.M. Suh, D. Cho, S. Lee, T.H. Lee, J.W. Jung, J. Lee, et al., Rationally designed TiO2 nanostructures of continuous pore network for fast-responding and highly sensitive acetone sensor, Small Methods 5 (2021) 2100941.

[7] J. Lee, H. Lee, T.-H. Bae, D. Cho, M. Choi, G. Bae, et al., 3D ZnO/ZIF-8 Hierarchical Nanostructure for Sensitive and Selective NO2 Sensing at Room Temperature, Small Struct. (2023) 2300503.

[8] M. Choi, J. An, H. Lee, H. Jang, J.H. Park, D. Cho, et al., High figure-of-merit for ZnO nanostructures by interfacing lowly-oxidized graphene quantum dots, Nat. Commun. 15 (2024) 1996.

[9] G. Seo, G. Lee, W. Kim, I. An, M. Choi, S. Jang, et al., Ultrasensitive biosensing platform for Mycobacterium tuberculosis detection based on functionalized graphene devices, Front. Bioeng. Biotechnol. 11 (2023).

[10] M. Choi, T.G. Novak, J. Byen, H. Lee, J. Baek, S. Hong, et al., Significantly enhanced thermoelectric performance of graphene through atomic-scale defect engineering via mobile hot-wire chemical vapor deposition systems, ACS Appl. Mater. Interfaces 13 (2021) 24304–24313.

[11] J. Lee, M. Park, Y.G. Song, D. Cho, K. Lee, Y.-S. Shim, et al., Role of graphene quantum dots with discrete band gaps on SnO 2 nanodomes for NO 2 gas sensors with an ultralow detection limit, Nanoscale Adv. 5 (2023) 2767–2775.

[12] J. Shin, G. Lee, M. Choi, H. Jang, Y. Lim, G.-S. Kim, et al., Atomically mixed catalysts on a 3D thin-shell TiO 2 for dual-modal chemical detection and neutralization, J. Mater. Chem. A 11 (2023) 18195–18206.

[13] P. Serrini, V. Briois, M. Horrillo, A. Traverse, L. Manes, Chemical composition and crystalline structure of SnO2 thin films used as gas sensors, Thin Solid films 304 (1997) 113–122.

[14] G. Neri, A. Bonavita, G. Micali, G. Rizzo, N. Pinna, M. Niederberger, et al., Effect of the chemical composition on the sensing properties of In2O3–SnO2 nanoparticles synthesized by a non-aqueous method, Sens. Actuators B: Chem. 130 (2008) 222–230.

[15] J.M. Suh, K.C. Kwon, T.H. Lee, C. Kim, C.W. Lee, Y.G. Song, et al., Edge-exposed WS2 on 1D nanostructures for highly selective NO2 sensor at room temperature, Sens. Actuators B: Chem. 333 (2021) 129566.

[16] V. Galstyan, A. Moumen, G.W. Kumarage, E. Comini, Progress towards chemical gas sensors: Nanowires and 2D semiconductors, Sens. Actuators B: Chem. 357 (2022) 131466.

[17] A. Saleem, Y. Zhang, M. Usman, M. Haris, P. Li, Tailored architectures of mesoporous carbon nanostructures: From synthesis to applications, Nano Today 46 (2022) 101607.

[18] S.Y. Yi, Y.G. Song, J.Y. Park, J.M. Suh, G.S. Kim, Y.-S. Shim, et al., Morphological evolution induced through a heterojunction of W-decorated NiO nanoigloos: synergistic effect on high-performance gas sensors, ACS Appl. Mater. Interfaces 11 (2019) 7529–7538.

[19] H. Ding, Y. Wei, Z. Wu, K. Tao, M. Ding, X. Xie, et al., Recent advances in gas and humidity sensors based on 3D structured and porous graphene and its derivatives, ACS Mater. Lett. 2 (2020) 1381–1411.

[20] A. Stein, F. Li, N.R. Denny, Morphological control in colloidal crystal templating of inverse opals, hierarchical structures, and shaped particles, Chem. Mater. 20 (2008) 649–666.

[21] S. Capone, A. Forleo, L. Francioso, R. Rella, P. Siciliano, J. Spadavecchia, et al., Solid state gas sensors: state of the art and future activities, J. Optoelectron. Adv. Mater. 5 (2003) 1335–1348.

[22] N. Sureshkumar, A. Dutta, Environmental gas sensors based on nanostructured thin films. Multilayer Thin Films-Versatile Applications for Materials Engineering, IntechOpen, 2020.

[23] S.-M. Yang, S.-H. Kim, J.-M. Lim, G.-R. Yi, Synthesis and assembly of structured colloidal particles, J. Mater. Chem. 18 (2008) 2177–2190.

[24] E.V. Shevchenko, D.V. Talapin, A.L. Rogach, A. Kornowski, M. Haase, H. Weller, Colloidal synthesis and self-assembly of CoPt3 nanocrystals, J. Am. Chem. Soc. 124 (2002) 11480–11485.

[25] J. Lee, Y. Jung, S.-H. Sung, G. Lee, J. Kim, J. Seong, et al., High-performance gas sensor array for indoor air quality monitoring: the role of Au nanoparticles on WO 3, SnO 2, and NiO-based gas sensors, J. Mater. Chem. A 9 (2021) 1159–1167.

[26] Z. Cai, Z. Li, S. Ravaine, M. He, Y. Song, Y. Yin, et al., From colloidal particles to photonic crystals: Advances in self-assembly and their emerging applications, Chem. Soc. Rev. 50 (2021) 5898–5951.

[27] J.H. Huh, K. Kim, E. Im, J. Lee, Y. Cho, S. Lee, Exploiting colloidal metamaterials for achieving unnatural optical refractions, Adv. Mater. 32 (2020) 2001806.

[28] R. Aveyard, B.P. Binks, J.H. Clint, Emulsions stabilised solely by colloidal particles, Adv. Colloid Interface Sci. 100 (2003) 503–546.

[29] Y.-S. Shim, H.Y. Jeong, Y.H. Kim, S.H. Nahm, C.-Y. Kang, J.-S. Kim, et al., Utilization of both-side metal decoration in close-packed SnO2 nanodome arrays for ultrasensitive gas sensing, Sens. Actuators B: Chem. 213 (2015) 314–321.

[30] A. Böker, J. He, T. Emrick, T.P. Russell, Self-assembly of nanoparticles at interfaces, Soft Matter 3 (2007) 1231–1248.

[31] I. Otsuka, M. Osaka, Y. Sakai, C. Travelet, J.-L. Putaux, R. Borsali, Self-assembly of maltoheptaose-block-polystyrene into micellar nanoparticles and encapsulation of gold nanoparticles, Langmuir 29 (2013) 15224–15230.

[32] J. Tian, J. Jin, F. Zheng, H. Zhao, Self-assembly of gold nanoparticles and polystyrene: a highly versatile approach to the preparation of colloidal particles with polystyrene cores and gold nanoparticle coronae, Langmuir 26 (2010) 8762–8768.

[33] J.M. Suh, Y.G. Song, J.H. Seo, M.S. Noh, M.G. Kang, W. Sohn, et al., Facile Formation of Metal–Oxide Nanocraters by Laser Irradiation for Highly Enhanced Detection of Volatile Organic Compounds, Small Struct. 4 (2023) 2300068.

[34] Y. Ke, X. Wen, D. Zhao, R. Che, Q. Xiong, Y. Long, Controllable fabrication of two-dimensional patterned VO2 nanoparticle, nanodome, and nanonet arrays with tunable temperature-dependent localized surface plasmon resonance, ACS nano 11 (2017) 7542–7551.

[35] H.-J. Cho, S.-J. Choi, N.-H. Kim, I.-D. Kim, Porosity controlled 3D SnO2 spheres via electrostatic spray: Selective acetone sensors, Sens. Actuators B: Chem. 304 (2020) 127350.

[36] A.K. Srivastava, J.S. Tawale, R. Verma, D. Agarwal, C. Sharma, A. Kumar, et al., Morphological evolution driven semiconducting nanostructures for emerging solar, biological and nanogenerator applications, Mater. Adv. 3 (2022) 8030–8062.

[37] G. Korotcenkov, V. Brinzari, A. Cerneavschi, M. Ivanov, V. Golovanov, A. Cornet, et al., The influence of film structure on In2O3 gas response, Thin Solid Films 460 (2004) 315–323.

[38] D. Han, L. Zhai, F. Gu, Z. Wang, Highly sensitive NO2 gas sensor of ppb-level detection based on In2O3 nanobricks at low temperature, Sens. Actuators B: Chem. 262 (2018) 655–663.

[39] T. Waitz, T. Wagner, T. Sauerwald, C.D. Kohl, M. Tiemann, Ordered mesoporous In2O3: synthesis by structure replication and application as a methane gas sensor, Adv. Funct. Mater. 19 (2009) 653–661.

[40] S.K. Lim, S.-H. Hwang, D. Chang, S. Kim, Preparation of mesoporous In2O3 nanofibers by electrospinning and their application as a CO gas sensor, Sens. Actuators B: Chem. 149 (2010) 28–33.

[41] N. Sui, P. Zhang, T. Zhou, T. Zhang, Selective ppb-level ozone gas sensor based on hierarchical branch-like In2O3 nanostructure, Sens. Actuators B: Chem. 336 (2021) 129612.

[42] N. Saito, H. Haneda, K. Watanabe, K. Shimanoe, I. Sakaguchi, Highly sensitive isoprene gas sensor using Au-loaded pyramid-shaped ZnO particles, Sens. Actuators B: Chem. 326 (2021) 128999.

[43] Y.-S. Shim, H.G. Moon, L. Zhang, S.-J. Yoon, Y.S. Yoon, C.-Y. Kang, et al., Au-decorated WO 3 cross-linked nanodomes for ultrahigh sensitive and selective sensing of NO 2 and C 2 H 5 OH, RSC Adv. 3 (2013) 10452–10459.

[44] J. Lee, D. Cho, H. Chen, Y.-S. Shim, J. Park, S. Jeon, Proximity-field nanopatterning for high-performance chemical and mechanical sensor applications based on 3D nanostructures, Appl. Phys. Rev. 9 (2022).

[45] Y. Tang, Y. Zhao, H. Liu, Room-temperature semiconductor gas sensors: Challenges and opportunities, ACS Sens. 7 (2022) 3582–3597.

[46] N. Yamazoe, Toward innovations of gas sensor technology, Sens. Actuators B: Chem. 108 (2005) 2–14.

[47] P. Zhang, C. Shao, X. Li, M. Zhang, X. Zhang, Y. Sun, et al., In situ assembly of well-dispersed Au nanoparticles on TiO2/ZnO nanofibers: A three-way synergistic heterostructure with enhanced photocatalytic activity, J. Hazard. Mater. 237 (2012) 331–338.

[48] Y. Zhang, D. Ma, J. Wu, Q. Zhang, Y. Xin, N. Bao, One–step preparation of CNTs/InVO4 hollow nanofibers by electrospinning and its photocatalytic performance under visible light, Appl. Surf. Sci. 353 (2015) 1260–1268.

[49] J.-S. Lee, A. Katoch, J.-H. Kim, S.S. Kim, Effect of Au nanoparticle size on the gas-sensing performance of p-CuO nanowires, Sens. Actuators B: Chem. 222 (2016) 307–314.

[50] A. Dey, Semiconductor metal oxide gas sensors: A review, Mater. Sci. Eng.: B 229 (2018) 206–217.

[51] S.D. Han, Y.G. Song, Y.-S. Shim, H.R. Lee, S.-J. Yoon, C.-Y. Kang, Preparation of Nanocolumnar In 2 O 3 Thin Films for Highly Sensitive Acetone Gas Sensor, J. Sens. Sci. Technol. 25 (2016) 383–387.

[52] P. Rai, Y.-S. Kim, H.-M. Song, M.-K. Song, Y.-T. Yu, The role of gold catalyst on the sensing behavior of ZnO nanorods for CO and NO2 gases, Sens. Actuators B: Chem. 165 (2012) 133–142.

[53] S. Neupane, R. Peverall, G. Richmond, T.P. Blaikie, D. Taylor, G. Hancock, et al., Exhaled breath isoprene rises during hypoglycemia in type 1 diabetes, Diabetes Care 39 (2016) e97–e98.

[54] J. Dadamio, S. Van den Velde, W. Laleman, P. Van Hee, W. Coucke, F. Nevens, et al., Breath biomarkers of liver cirrhosis, J. Chromatogr. B 905 (2012) 17–22.

[55] T. Qin, H. Liu, Q. Song, G. Song, H.-z Wang, Y.-y Pan, et al., The screening of volatile markers for hepatocellular carcinoma, Cancer Epidemiol., Biomark. Prev. 19 (2010) 2247–2253.

[56] R.A. Potyrailo, Multivariable sensors for ubiquitous monitoring of gases in the era of internet of things and industrial internet, Chem. Rev. 116 (2016) 11877–11923.

[57] S.-W. Park, S.-Y. Jeong, Y.K. Moon, K. Kim, J.-W. Yoon, J.-H. Lee, Highly selective and sensitive detection of breath isoprene by tailored gas reforming: a synergistic combination of macroporous WO3 spheres and Au catalysts, ACS Appl. Mater. Interfaces 14 (2022) 11587–11596.

Junho Hwang received a Master's degree in the Department of Mechanical Design Engineering from Kookmin University in 2018. Since 2020, He is currently a Ph.D. candidate in the Department of Materials Science and Engineering at Yonsei University under the supervision of Prof. Wooyoung Lee. His research focuses on micro/nanostructured materials and their large-area synthesis methods for gas sensing applications.

See-Hyung Park received a Bachelor's degree in the advanced material engineering at Silla University in 2023. Since 2023, He is currently a M. S. candidate in the School of Energy, Materials & Chemistry Engineering at Korea University of Technology & Education (KOREATECH). under the supervision of Prof. Young-Seok Shim. His research focuses on micro/nanostructured materials and their large-area synthesis methods for gas sensing applications.

Young-Seok Shim is currently an Assistant Professor in the School of Energy, Materials & Chemical Engineering at Korea University of Technology & Education (KOREATECH), Korea since 2022. Before joining the KOREATECH, he was an Assistant Professor at Silla

University (2020–2022). He received his Ph.D. (2016) degree in the Department of Materials Science & Engineering from Yonsei University, Korea. From 2016–2017, he was a postdoctoral research associate at the Electronic Materials Center at Korea Institute of Science & Technology (KIST). From 2018–2020, he joined in the Department of Materials Science & Engineering at Korea Advanced Institute of Science and Technology (KAIST) as a postdoctoral researcher. His research interests are micro/nanostructured materials and their large-area synthesis methods for gas sensing applications. He has published more than 60 international journal articles (SCI indexed).

Sungwoo Sohn received a Bachelor's degree in the School of Energy, Materials & Chemical Engineering at Korea University of Technology & Education (KOREATECH) in 2023. Since 2023, He is currently a M. S. candidate in the Department of Materials Science and Engineering at Yonsei University under the supervision of Prof. Wooyoung Lee. His research focuses on micro/nanostructured materials and their large-area synthesis methods for gas sensing applications.

Jae Han Chung is a combined bachelor-master's candidate under the supervision of Prof. Young-Seok Shim at School of Energy, Materials & Chemical Engineering at Korea University of Technology & Education (KOREATECH). His research interests are the fabrication of nanostructured metal oxide and their applications to various devices including sensor and electrochromic devices.

Yun-Haeng Cho is currently a combined bachelor-master's candidate in the School of Energy, Materials & Chemical Engineering at Korea University of Technology & Education (KOREATECH) under the supervision of Prof. Young-Seok Shim. His research focuses on micro/nanostructured materials and their large-area synthesis methods for gas sensing applications.

Jinho Lee received his Ph.D. degree from Department of Materials Science and Engineering at Korea Advanced Institute of Science and Technology (KAIST) in 2023. He is currently working as a post-doctoral fellow in Department of Materials Science and Engineering at Korea Advanced Institute of Science and Technology (KAIST).

Myungwoo Choi received his Ph.D. degree from Department of Materials Science and Engineering at Korea Advanced Institute of Science and Technology (KAIST) in 2023. He is currently working as a post-doctoral fellow in Department of Materials Science and Engineering at Korea University. His research focuses on the fabrication of nanostructured

functional materials and exploring their applications, such as gas sensors, thermal sensors, thermoelectric devices, and electronic devices.

Gye Hyeon Lee is currently a master's candidate in the joint graduate program with the Korea Research Institute of Chemical Technology (KRICT) and the Department of Materials Science and Engineering at Korea University under the supervision of Dr. Donghwi Cho and Prof. Seokwoo Jeon. His research focuses on micro/nanostructured materials for gas sensing applications.

Donghwi Cho is a senior researcher of the Advanced Materials Division at the Korea Research Institute of Chemical Technology (KRICT) in Korea (2021~present). He is also the assistant professor of Advanced Materials and Chemical Engineering at the University of Science and Technology in Korea (2024~present). Before joining KRICT, He received his Ph.D. degree in Materials Science and Engineering at KAIST in 2020 and started to work at Querrey Simpson Institute for Bioelectronics of Northwestern University as a postdoctoral associate (2020–2021). His research topic spans various domains, including 3D nanopatterning, nanoarchitectonics of functional materials, and development of the advanced bioelectronic systems. He has published over 40 international publications.

Kwangjae Lee received his Ph.D. degree from Department of Electrical and Computer Engineering of Korea University in 2014. Now he is a professor of Department of Information Security Engineering in Sangmyung University, since 2017.

Wooyoung Lee is the Underwood distinguished professor of the Department of Materials Science and Engineering at Yonsei University in Korea. He is also the Director of the Center for Super Critical Material Industrial Technology, National Core Materials Research Center and the institute of Korea Initiative for Fostering University of Research and Innovation. He is the President of The Korean Magnetics Society and a regular member of the National Academy of Engineering of Korea. In recent years, his research interests have centered on hydrogen sensors, various metal oxide semiconducting gas sensors, and breath analyzers. He is also studying rare-earth permanent magnets and thermoelectric materials and devices. He has received a number of awards in nano-related research areas including a Prime Minister Award (2023) in Nano Korea 2023, SeAH-Haiam Fellowship Award (2018) in The Korean Institute of Metals and Materials and a Service Merit Medal (2008) from the Government of Korea due to his contribution to the development of intellectual properties. He has authored and co-authored over 280 publications and has edited three special books on nanostructured materials and devices.